Journal of Materials Chemistry C

ROYAL SOCIETY OF CHEMISTRY

PAPER

Cite this: J. Mater. Chem. C, 2020, 8, 7882

A probe of the radiation field magnetic component based on octahedral Yb^{3+} in the CaNbGa garnet – CNGG – single crystal†

Jorge Omar Álvarez-Pérez, José María Cano-Torres, María Dolores Serrano, Concepción Cascales and Carlos Zaldo *

Received 30th March 2020, Accepted 30th April 2020

DOI: 10.1039/d0tc01608j

rsc.li/materials-c

In a disordered Yb^{3+}-doped CaNbGa garnet – CNGG – single crystal, it is shown that octahedral Yb centers exist up to a solubility limit of about 5×10^{18} cm^{-3} in addition to the well known dodecahedral Yb which incorporates to a much larger density $\sim 10^{21}$ cm^{-3}. Despite the low density of the octahedral Yb, the presence of a symmetry center for this garnet site forbids electric dipole (ED) transitions, thus magnetic dipole (MD) spectroscopic contributions are observed with an intensity similar to that of ED ones. Because of the easy growth of this garnet, the potential application of these two contributions for probing the magnetic field component radiated by plasmonic structures is discussed on the basis of time-resolved spectroscopy, since ED Yb^{3+} photoluminescence is about one order of magnitude faster than MD $^2F_{5/2} \rightarrow {}^2F_{7/2}$ ($\Delta J = +1$) emissions for the 0.3 at%Yb:CNGG crystal. Channels appropriated for room temperature operation can be excited at λ_{EXC} = 960.3 nm, while sensed at λ_{EMI} = 1022 nm for the short-lived ED reference channel and λ_{EMI} = 998, 1011, 1068 or 1080 nm for the long-lived MD signal channel.

1. Introduction

Energy levels of trivalent lanthanides (Ln^{3+}) are characterized by $^{2S+1}L_J$ multiplets further split by the crystal field (CF) of a host in m_J levels. Intraconfigurational electronic transitions between these multiplets are most often induced by light–matter interactions mediated by electric fields through forced electric dipole (ED) transitions, but also include magnetic dipole (MD) interactions, particularly notable for transitions between multiplets with $\Delta J = 0$ or ± 1.[1] Although it is usually assumed that MD transitions are $\sim 10^5$ times weaker than ED ones, their relative intensity in fact depends on the specific selection rules. In hosts where ED transitions are weak or even strictly forbidden, as when Ln^{3+} are incorporated at sites with a center of symmetry, the intensity of MD transitions can be dominant.

Stimulated by recent advances in optical plasmonic-based metamaterials and nanophotonics, a variety of ways to exploit MD transitions of Ln^{3+} have been proposed: theoretically, as the building blocks for homogeneous negative index materials,[2] or experimentally, as probes for the study of local magnetic fields in metamaterials, in a very simple approach that consists of placing the MD probe at the metamaterial surface, and if this resonance frequency corresponds to the spectral range of the field enhancement, spectral changes in intensity or shape may be observed in comparison with other magnetic dipoles outside the system or with some reference ED emission in the same system.[3–7] Furthermore, experimental studies by using the competition between ED and MD processes have shown the way for achieving a strong enhancement of MD emission[8] and also to broadly tune the emission spectra.[9]

For the above indicated sensing purposes, previous studies have involved mainly the visible $^5D_0 \rightarrow {}^7F_1$ MD transition of Eu^{3+}, in probing systems based on Eu-doped Y_2O_3 thin films,[7–9] dispersions of Eu-doped organic systems in polymeric thin films,[3,4,6] or Eu-doped Y_2O_3 NPs (about 60 nm).[10] The specific advantage of using Eu^{3+} is the coexistence of the nearly pure MD $^5D_0 \rightarrow {}^7F_1$ ($\lambda \approx 590$ nm) transition and the ED $^5D_0 \rightarrow {}^7F_2$ ($\lambda \approx 615$ nm) transition used as the reference. Other Ln^{3+} emissions which have been tested with the same aim are mixed MD–ED transitions in the near-infrared (NIR) range, for instance the overlapping $^4F_{9/2} \rightarrow {}^6F_{11/2} + {}^6H_{9/2}$ ($\lambda \approx 734$ nm) emissions of Dy^{3+},[11] the also overlapping $^1G_4 \rightarrow {}^3H_5$ ($\lambda \approx 784$ nm) and $^3H_4 \rightarrow {}^3H_6$ ($\lambda \approx 800$ nm) emissions of Tm^{3+},[11] or the $^4I_{13/2} \rightarrow {}^4I_{15/2}$ ($\lambda \approx 1.5$ μm) transition of Er^{3+},[12] in all cases by using the corresponding doped Y_2O_3 thin films.

Instituto de Ciencia de Materiales de Madrid, Consejo Superior de Investigaciones Científicas, c/Sor Juana Inés de la Cruz 3, 28049 Madrid, Spain.
E-mail: cezaldo@icmm.csic.es

† Electronic supplementary information (ESI) available: (i) Detailed comparative optical spectroscopy of dodecahedral and octahedral Yb^{3+} centers in CNGG crystals. (ii) Detailed procedures of crystal field analyses applied to octahedral Yb^{3+} centers in 0.3 at%Yb:CNGG crystals. (iii) Crystal field splitting of ^2F_J Yb^{3+} levels and the barycenter law. See DOI: 10.1039/d0tc01608j

The near-infrared (NIR) range from 800 to 1100 nm has several advantages over other spectral regions. As compared to the visible (characteristic of Eu^{3+}), micron-sized plasmonic nanostructures are much easier to fabricate than nano-sized ones and their resonances exhibit higher-quality factors due to lower ohmic losses. However, as compared with the $^4I_{13/2} \rightarrow {}^4I_{15/2}$ Er^{3+} transition at $\lambda \approx 1.5$ μm, emissions at $\lambda < 1100$ nm can be observed using standard Si photodetector technology, which simplifies the detection process. Moreover, among MD Ln^{3+} emissions at this wavelength range, those that can be pumped at the NIR will be the better candidates to be used. From the above considerations the $^2F_{5/2} \leftrightarrow {}^2F_{7/2}$ transitions of Yb^{3+} (typically $\lambda_{EXC} \approx$ 940–980 nm and $\lambda_{EMI} \approx$ 980–1060 nm) in a centrosymmetric crystal site are very interesting options. The simple two-state energy structure of Yb^{3+} means that MD emission can account for a significant contribution to the overall decay. In fact, relatively long Yb^{3+} lifetime (τ) characteristics of MD transitions have been measured for Yb-doped BaF_2 and SrF_2 fluorites (τ = 9.72 ms and 8.20 ms, respectively), as well as for Rb_2NaYF_6 elpasolite (τ = 10.84 ms) crystals, with Yb^{3+} at centrosymmetric sites of cubic eightfold and perfect octahedral coordination,[13] respectively, in both cases with calculated MD branching ratios of ~50%.[12]

Cubic garnets $A_3M_2N_3O_{12}$ with space group $Ia\bar{3}d$ (No. 230) offer simultaneously non centrosymmetric dodecahedral 24c sites (A) and octahedral 16a centrosymmetric sites (M) to host Ln. An illustration of the garnet structure can be seen in the general view given in Fig. 1a. Fig. 1b shows the coordination of dodecahedral AO_8 and octahedral MO_6 garnet sites. Further drawings showing other atomic arrangements can be seen for instance in ref. 14. The Ln^{3+} distribution over 24c and 16a garnet sites is a topic which has been addressed with several purposes and under different approaches.[15–23] The main factor governing the site preference of Ln^{3+} in the garnet structure is the ionic size, in such a way that garnets with any Ln^{3+} cation occupying the dodecahedral 24c site are known,[15] and only the smallest size Ln^{3+} cations, typically Dy^{3+} to Lu^{3+} and also Y^{3+} or Sc^{3+}, are able to enter into the octahedral 16a site, even up to its complete filling, but in this case a 24c cation with a considerably large size, for example Ca^{2+} in the germanate series $Ca_3Ln_2Ge_3O_{12}$,[18] including $Ca_3Y_2Ge_3O_{12}$,[20] is required, thus the relative sizes of 24c and 16a cations also play a role. The presence of Yb^{3+} in both garnet sites would offer the possibility of having the MD probe and ED reference ions in the same tested volume minimizing uncertainties related to excitation and detection processes, but so far the properties of Yb coexisting in both garnet sites have not been properly documented. Either the studies are limited to crystallographic aspects,[16,17,20] or the spectroscopic-based proposals[21,23] are not soundly supported by crystallographic data and/or crystal field (CF) interaction calculations.

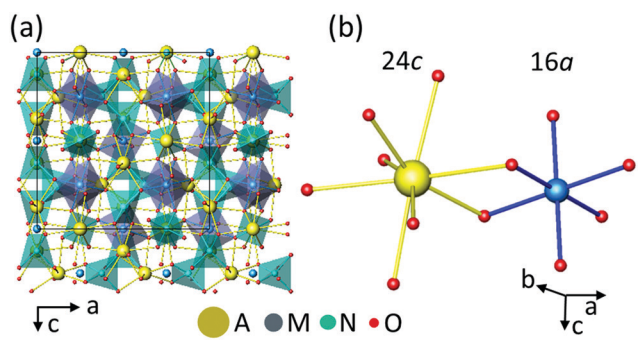

Fig. 1 (a) General view of the $A_3M_2N_3O_{12}$ garnet structure. (b) Oxygen coordinations of the AO_8 24c dodecahedra and MO_6 16a octahedra.

In this work we present the first report and characterization of the $^2F_{5/2}(n') \leftrightarrow {}^2F_{7/2}(n)$ MD transitions of Yb^{3+} at the octahedral 16a (centrosymmetric C_{3i} symmetry) site of the CaNbGa garnet (thereafter CNGG). The host selection is based on the large Ca^{2+} ionic size filling the dodecahedral site, see before, while a large variety of ionic filling (Nb^{5+}, Ga^{3+} and even vacancies) is found for the octahedral and tetrahedral sites of this garnet composition. The occupancy of the 24c dodecahedral site of the CNGG garnet by Yb^{3+} is well documented from both crystallographic and spectroscopic points of view.[24–27]

The emphasis of the present work is the study of Yb^{3+} in the octahedral 16a CNGG garnet site. Through low temperature (6 K) optical absorption (OA) and photoluminescence (PL) spectra followed by the modeling of CF interactions, it has been possible to establish the sequence of 16a Yb^{3+} energy levels as a well-separated set with regards to those of Yb^{3+} at the 24c dodecahedral site. The lifetime associated with the 16a Yb^{3+} $^2F_{5/2} \rightarrow {}^2F_{7/2}$ MD emissions has been also measured, and the MD branching ratio has been calculated as β_{MD} = 50%, a value that equals those of previously indicated for Yb^{3+} in centrosymmetric sites of fluoride-based hosts.[12] Furthermore, by using their different kinetics, ED and MD Yb^{3+} PL contributions have been separated even at room temperature (RT), opening the possibility of its application as a sensor for the magnetic field radiation in plasmonic systems.

2. Methods

2.1 Crystal growth

The crystal precursor polycrystalline material with a nominal cationic composition $Ca_{2.991}Yb_{0.009}Nb_{1.6875}Ga_{3.1875}$ (0.3 at%Yb: CNGG) was prepared by mixing $CaCO_3$ (Alfa Aesar 99.5%), Yb_2O_3 (99.99%, acquired through Shangai Zimei International Co., Ltd), Nb_2O_5 (Aldrich 99.9%) and Ga_2O_3 (Aldrich 99.99%) in a 36.33 : 0.21 : 27.21 : 36.25 weight% ratio. This off-stoichiometry formula is within the composition range with congruent melting that allows garnet crystal growth from the melt.[28] The mixture was heated in air to 1648–1673 K for several hours with intermediate regrinding. The garnet phase purity of the synthesized crystal precursor material was checked at RT using powder X-ray diffraction using a Bruker AXS D-8 Advance diffractometer with Cu K_α radiation. From this polycrystalline powder the single crystal was grown in air by the Czochralski technique. For this purpose we used a Cyberstar crystal growth equipment incorporating a radiofrequency (RF) coil fed by a Huttinger TruHeat MF 3020 power supply operated at 9.2 kHz. The crucible (40 mm in diameter and height) was made of platinum, and a

platinum wire was used as the seed, which was rotated and pulled simultaneously. Samples for optical purposes were obtained by crystal cutting and polishing using conventional methods.

2.2 Structural and compositional analyses

Due to the low Yb^{3+} doping (nominally 0.3 at% with regard to the dodecahedral site occupancy) of the currently studied 0.3 at%Yb:CNGG crystal, its structure should be very similar to that described for the undoped CNGG single crystal in one of our previous studies.[14] So, we shall adopt the crystal formula previously determined by the refinement of single crystal X-ray diffraction (XRD) data, *i.e.* $\{Ca_{0.985}\square_D\}_3[Nb_{0.625}Ga_{0.372}\square_O]_2$-$(Ga_{0.821}Nb_{0.102}\square_T)_3O_{12}$, $\square$ stating for vacancies at 24c dodecahedral (curly brackets), 16a octahedral (square brackets) and 24d tetrahedral (parentheses) sites.

The low concentration of Yb in the studied garnet prevents their compositional determination using XRD or X-ray fluorescence methods. However, these methods were successfully used for heavily (>10 at%) Yb-doped crystals. Thus, the actual Yb content of the used 0.3 at%Yb:CNGG crystal was determined by comparison of the integrated RT OA in this and in heavily Yb-doped crystals. This methodology provides a 0.08 at%Yb content for the grown crystal with regards to the dodecahedral occupancy.

2.3 Spectroscopic techniques

OA in the visible and NIR region was determined by using a Varian spectrophotometer, model Cary 5E, with a limiting spectral resolution of 0.04 nm at $\lambda \approx 1000$ nm. An extensive 6 K OA study in the whole visible region using a thick (≈5.1 mm) 0.3 at%Yb:CNGG sample discarded the contamination with any Ln different to the studied Yb^{3+}. PL was excited either in a continuous wave (cw) with a tunable Ti-sapphire laser or pulsed (10 Hz) with a tunable Quanta-Ray MOPO-HF system providing ns laser pulses. PL light was dispersed in a SPEX (f = 34 cm) spectrometer and detected using a 77 K cooled Ge photodiode in cw experiments, or with a Hamamatsu InP/InGaAs phototube (model H10330A-75) in lifetime measurements and time-resolved spectroscopy. In cw PL experiments the laser beam was chopped at ≈200 Hz and the PL signal recovered with a lock-in amplifier. Yb^{3+} lifetime measurements were carried out using a thin crystal plate (60 μm) in order to minimize emission reabsorption. Time-resolved spectroscopy was discriminated by a Stanford Research SR400 photon counter. For 6 K optical spectroscopic measurements a He close-cycle cryostat connected to a suitable temperature controller was used.

3. Results

The OA and PL spectra of Yb^{3+} in the CNGG host originate from electronic transitions between ground $^2F_{7/2}$ and excited $^2F_{5/2}$ Yb^{3+} multiplets. Both, the D_2 and C_{3i} local symmetries of the dodecahedral 24c and octahedral 16a garnet sites, respectively, split these multiplets into four $^2F_{7/2}$ (n = 0, 1, 2, 3) and three $^2F_{5/2}$ (n' = 0′, 1′, 2′) Kramers doublets.

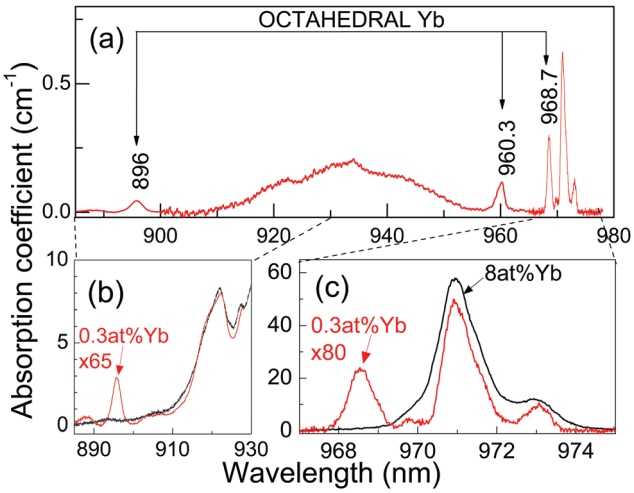

Fig. 2 (a) 6 K optical absorption spectrum of the 0.3 at%Yb:CNGG crystal (red line), and its comparison with that of the 8 at%Yb:CNGG crystal (black line) for (b) $^2F_{7/2}(0) \rightarrow {}^2F_{5/2}(2')$ and (c) $^2F_{7/2}(0) \rightarrow {}^2F_{5/2}(0')$ Yb^{3+} transitions.

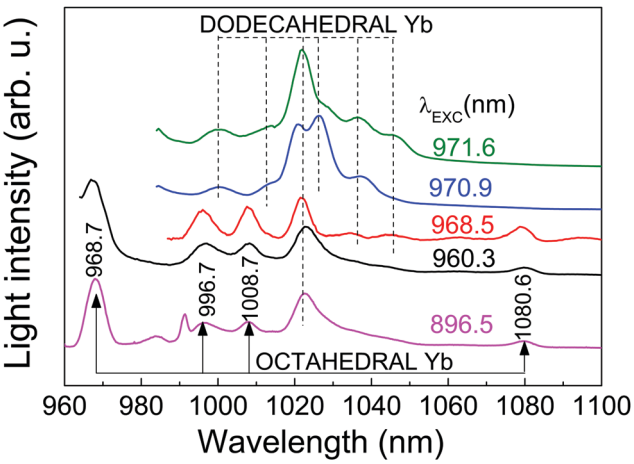

Fig. 3 Comparison of the 6 K photoluminescence spectra assigned to the octahedral 16a (λ_{EXC} = 896.5, 960.3 or 968.5 nm) and dodecahedral 24c (λ_{EXC} = 970.9 and 971.6 nm) Yb^{3+} in the 0.3 at%Yb:CNGG single crystal.

The Yb^{3+} spectra of heavily doped (>1 at%Yb) CNGG crystals have been previously studied in detail.[14,24–27] So far, the crystallographic and spectroscopic studies only provided evidence for Yb incorporation in the dodecahedral 24c site. The 6 K OA and PL spectra consist in inhomogeneously and thermally broadened bands which hamper the accurate determination of some Yb^{3+} energy levels. Fig. 2 and 3 show selected examples of the optical contributions of dodecahedral Yb in CNGG, while a more extensive dodecahedral Yb spectroscopic review is provided in the ESI.†

The only well resolved band in the 6 K spectra of 8 at%Yb:CNGG crystals is $^2F_{7/2}(0) \leftrightarrow {}^2F_{5/2}(0')$ (shortly, $0 \leftrightarrow 0'$) at λ = 970.9 nm (see Fig. 2c). Even this band is largely broadened by the different crystalline environments coexisting around the dodecahedral 24c site of Yb^{3+}, since the spectral position of this $0 \leftrightarrow 0'$ transition is mainly related to the electric charge of cations/vacancies occupying the two edge-sharing tetrahedra

at the shortest distance (~3.12 Å) from the central 24c Yb^{3+}.[24] In fact, the small OA band at λ = 973 nm corresponds to a dodecahedral Yb^{3+} center linked to a vacant edge-sharing tetrahedron.[24]

The 6 K OA (Fig. 2) and PL (Fig. 3) spectra of the 0.3 at%Yb:CNGG crystal show bands not observable in the corresponding spectra for heavily doped >1 at%Yb:CNGG crystals. The new well-resolved OA bands peak at 968.7 nm (10 323 cm^{-1}), 960.3 nm (10 413 cm^{-1}) and 896 nm (11 161 cm^{-1}), while characteristic PL emissions at 968.7 nm, 996.7 nm, 1008.7 nm and 1080.6 nm are observed when exciting any of the three above listed OA bands (see Fig. 3). The absorption intensity of this new band set reaches 40% when the 968.7 nm new OA is compared with that of the dodecahedral Yb 0 ↔ 0′ transition at λ = 970.9 nm, see Fig. 2c. These new OA and PL band sets indicate the actual presence of a second type of Yb center coexisting in the garnet structure with the main dodecahedral Yb^{3+} center but with a much lower solubility limit, and thus, although present with low density, its contribution is not observable in the spectrum of the heavily doped Yb:CNGG crystals. In the following we show that this new center is compatible with the assumption of Yb^{3+} located at the octahedral 16a garnet site, and hereafter we shall refer to it as octahedral Yb.

Therefore, from the OA and PL bands experimentally determined for the octahedral Yb^{3+} center in CNGG, the complete set of Yb^{3+} energy levels can be established as 0, 290, 410 and 1069 cm^{-1} for the ground $^2F_{7/2}$ (0, 1, 2, 3), and 10 323, 10 413 and 11 161 cm^{-1} for the excited $^2F_{5/2}$ (0′, 1′, 2′) multiplets.

In a further attempt to correlate these energy levels with the octahedral C_{3i} ($\equiv S_6$) symmetry of the 16a garnet site, a parametrization of CF effects in this site has been carried out. Since the large number of CF parameters accounting for the C_{3i} symmetry makes it unrealistic for any CF modeling to reproduce the sequence of Yb^{3+} energy levels, the often followed "descent of symmetry" procedure has considered the tetragonal bypiramidal D_{4h} symmetry as the better approach, *i.e.* the higher symmetry polyhedron with coordination number CN = 6 that can be regarded as a distortion of an octahedron O_h whose fourfold rotation axis is chosen as the main axis. For the D_{4h} symmetry the CF potential is described by B_0^2, B_0^4, B_4^4, B_0^6 and B_4^6 CF parameters, preliminary O_h, B_0^4 and B_0^6 being the only independent parameters whose values were initially obtained by using the semi-empirical Simple Overlap Model.[29] Details of the procedure for the CF parametrization of 16a Yb^{3+} energy levels in CNGG are given in the ESI.† The energy levels of 16a Yb^{3+} in CNGG were adequately reproduced by using the set of free ion and D_{4h} CF parameters included in Table 1.

The $^2F_{5/2}$ Yb^{3+} PL intensity decay kinetics has been also studied as a further signature of the different symmetry of the two (octahedral and dodecahedral) Yb^{3+} centers observed in the 0.3 at%Yb:CNGG crystal. The $^2F_{5/2}$ Yb^{3+} PL time constant (τ) after 970–973 nm excitation through the $^2F_{7/2}(0) \rightarrow {}^2F_{5/2}(0')$ Yb^{3+} transition in the dodecahedral centers was shown to vary in the τ = 800–450 μs range depending on the selected excitation/emission wavelength, *i.e.* the inhomogenously modified dodecahedral center selected.[24] The increase of the Yb concentration further reduces this time constant. An example of the PL kinetics is shown in Fig. 4a.

Table 1 Free ion (E^0 and ζ) and D_{4h} (B_0^2, B_0^4, B_4^4, B_0^6 and B_4^6) crystal field parameters (in cm^{-1}) used to reproduce the sequence of $^2F_{7/2}$ and $^2F_{5/2}$ energy levels of 16a Yb^{3+} in the CNGG crystal

Parameter		Yb^{3+} energy levels		
		Label	Observed (cm^{-1})	Calculated (cm^{-1})
E^0	4809.4	$^2F_{7/2}(0)$	0	−3.4
ζ	2905.3	$^2F_{7/2}(1)$	290	288
B_0^2	−64	$^2F_{7/2}(2)$	410	409
B_0^4	2375	$^2F_{7/2}(3)$	1069	1076
B_4^4	1844	$^2F_{5/2}(0')$	10 323	10 328
B_0^6	−210	$^2F_{5/2}(1')$	10 413	10 416
B_4^6	251	$^2F_{5/2}(2')$	11 161	11 153

The octahedral Yb center of the 0.3 at%Yb:CNGG crystal exhibits completely different PL intensity decay kinetics, see Fig. 4b. Its time extent widely covers the 10 ms range, it is more sensitive to the sample heating from 6 K to RT than in the dodecahedral case and most often a non-single exponential behavior is observed. The PL decay kinetics excited at λ_{EXC} = 960.3 nm are basically independent of the monitored wavelength

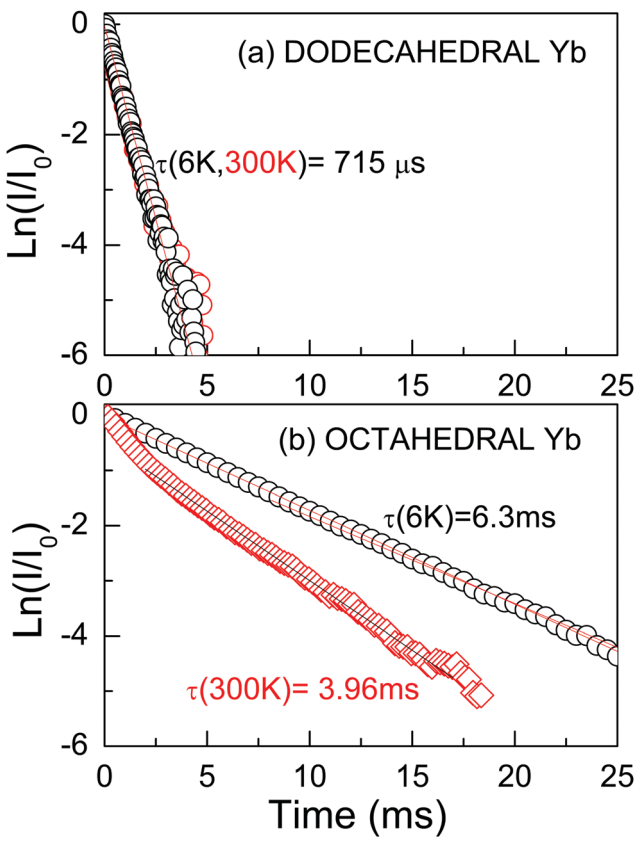

Fig. 4 Comparison of the $^2F_{5/2}$ photoluminescence intensity decay of the (a) dodecahedral 24c Yb^{3+} center, λ_{EXC} = 970.9 nm and λ_{EMI} = 1022 nm, and (b) octahedral 16a Yb^{3+} center, λ_{EXC} = 960.3 nm and λ_{EMI} = 1080.6 nm, of the 0.3 at%Yb:CNGG crystal. The points are the experimental results measured at 6 K (black points) and 300 K (red points). The lines are the fits of the long component of the corresponding decay.

(λ_{EMI} = 968.7 nm, 996.7 nm, 1008.7 nm or 1080.6 nm), see the ESI† (Fig. S4). They most typical show a fast decay for $t < 2$ ms and later a rather slow decay for the rest of the monitored time. This is understood as the overlapped contributions of the dodecahedral (short-lived) and octahedral (long-lived) Yb^{3+} centers. The long time tail of the decay can be fit to a single exponential law with a time constant $\tau \approx 6$–7 ms at 6 K and $\tau \approx 4$ ms at 300 K, *i.e.* the PL lifetime of the octahedral Yb^{3+} center is nearly one order of magnitude larger than that of the dodecahedral Yb one in the same crystal. This strong difference is consistent with the expected ED or MD Yb^{3+} PL contributions of these centers. For the non-centrosymmetric 24c D_2 dodecahedral site the contribution of ED transitions is expected to dominate the PL emission; thus the obtained $^2F_{5/2}$ Yb^{3+} lifetime is in the range observed for crystals hosting Yb^{3+} in similar non-centrosymmetric sites, like YAG, $\tau \approx 950$ μs,[30] $NaLn(WO_4)_2$ $\tau \approx 300$–500 μs,[31] or $LnVO_4$ $\tau \approx 250$–350 μs.[32] However, as stated in the Introduction, the presence of a center of symmetry forbids ED transitions, thus MD ones are observed with similar or even larger intensities than for the ED contributions. Such MD transitions are characterized by long PL lifetimes, thus the much larger lifetime obtained for the so-called Yb octahedral center may be regarded as the ultimate probe of the occupancy by Yb^{3+} in the centrosymmetric 16a crystal site of the CNGG host.

Once the origin of the described OA and PL features of the 0.3 at%Yb:CNGG crystal has been clarified thanks to 6 K spectroscopy, its application as a probe of plasmonic induced radiation fields requires operation at RT. Fig. 5 shows a comparison of the OA spectra corresponding to 0.3 at% and 11.6 at%Yb:CNGG crystals, the spectroscopy of the latter being purely dominated by the dodecahedral Yb^{3+} contributions. It is obvious that excitation of the octahedral Yb^{3+} center at RT through its $0 \rightarrow 0'$ transition at λ = 968.7 nm is not possible because with increasing temperature the relative intensity of this band decreases and overlaps with the $0 \rightarrow 0'$ (at λ = 972.3 nm) band tail corresponding to the dodecahedral Yb^{3+} center. However, the comparison of the spectra at both Yb doping concentrations shows that the octahedral Yb^{3+} $0 \rightarrow 1'$ transition at λ = 960.3 nm is clearly resolved from the background dodecahedral Yb contribution, the latter amounts to about 50% at this wavelength. Although the standard (integrated over time) cw PL spectra show little difference for excitation at the octahedral Yb^{3+} (λ = 960.3 nm) or in the side bands corresponding to the dodecahedral Yb^{3+} centers (see Fig. S3, ESI†), taking advantage of the different PL kinetics of both Yb^{3+} garnet centers, time-resolved spectroscopy can disclose the separate contributions of these two Yb^{3+} garnet centers.

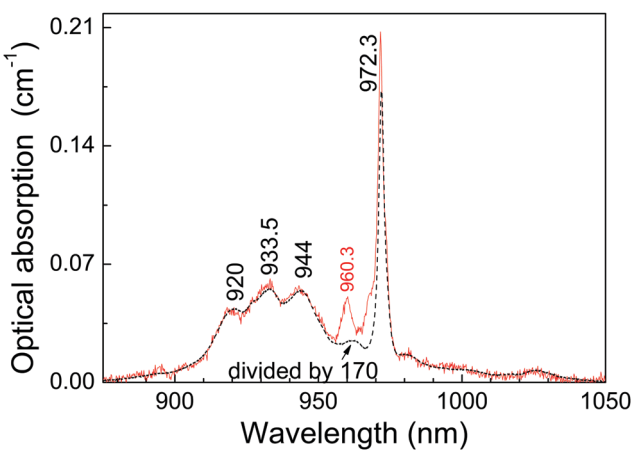

Fig. 5 Comparison of the 300 K OA spectra of 0.3 at%Yb:CNGG (red continuous line) and 11.6 at%Yb:CNGG (black dashed line) crystals. The spectral intensity of the latter crystal is divided by a factor of 170 to equal the intensity of the dodecahedral Yb^{3+} bands (920–944 nm) in both crystals.

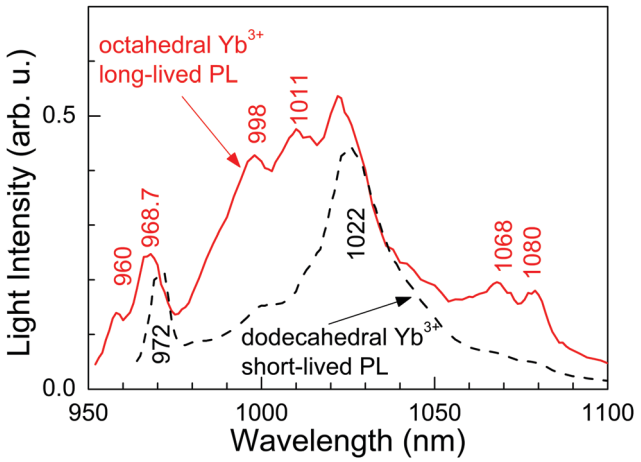

Fig. 6 300 K time-resolved photoluminescence emission of the 0.3 at%Yb:CNGG crystal after excitation at λ = 960.3 nm for different delay and gate times. Gate width of 250 μs delay 5 μs after laser pulse excitation (representative of the dodecahedral Yb^{3+} contribution, black dashed line) and gate width of 8 ms delay 2.5 ms (representative of the octahedral Yb^{3+} center, red continuous line).

Fig. 6 shows the RT time-resolved PL emission obtained for different delays and gate widths after the laser pulse (<5 ns of duration, tuned at λ = 960.3 nm) excitation. For short times (5 μs of delay and 250 μs of gate width) the PL is dominated by the short-lived ED contributions of the dodecahedral Yb^{3+} center. Correspondingly, the emission spectrum shows a broad peak at 1022 nm characteristic of the PL observed in highly doped Yb:CNGG,[24,26] which is also shown in Fig. 3 (λ_{EXC} = 971.6 nm). However, over a long time (2.5 ms of delay and 8 ms of gate width) the spectrum is quite different, and matches the emission of the octahedral Yb^{3+} shown in Fig. 3. Although the contribution of the λ = 1022 nm band is still present, this PL spectrum contains four well resolved emissions at λ = 998, 1011, 1068 and 1080 nm, with intensities 2.80, 2.56, 2.94 and 3.76 times those corresponding to the dodecahedral Yb^{3+} contributions at the same wavelengths, respectively. The origin of the 1068 nm RT emission is related to the thermal redistribution of the $^2F_{5/2}$ electronic population, and corresponds to the $^2F_{5/2}(1') \rightarrow {}^2F_{7/2}(3)$ transition of the octahedral Yb^{3+} center.

4. Discussion

From 6 K OA and the excitation/emission PL spectra shown in Fig. 2 and 3, it has been disclosed that along the predominant

dodecahedral Yb^{3+} optical center associated with 24c D_2 symmetry in YAG-like garnets, another minority Yb^{3+} center with very different spectroscopic characteristics coexists in the 0.3 at%Yb:CNGG crystal.

Several CF considerations support the above conclusion. On one side, the experimental energies determined for the m_J levels of the so called 16a octahedral Yb^{3+} center are well reproduced by using a CF parameter set describing a centrosymmetric center, see Table 1. On the other side, the absolute CF splittings of 1069 cm^{-1} and 838 cm^{-1} for ground $^2F_{7/2}$ and excited $^2F_{5/2}$ Yb^{3+} multiplets and their corresponding barycenters, lying at 442 cm^{-1} and 10 632 cm^{-1} energies, respectively, are consistent with those found in other 6-fold oxygen coordinated Yb ionic oxides: in Yb-doped sexquioxides the $^2F_{7/2}$ splitting ranges from 1193 cm^{-1} in Lu_2O_3,[33] to 1076 cm^{-1} in Sc_2O_3.[34] $\Delta E(^2F_{7/2})$ = 1023 cm^{-1} is found for $Ca_4YO(BO_3)_3$ (with 6O-Yb-2B coordination),[35] 964 cm^{-1} in Y_2SiO_5,[34] and 900 cm^{-1} in $Ba_3Lu(BO_3)_3$.[34] Smaller $\Delta E(^2F_{7/2})$ values in 6-fold oxygen coordinated Yb compounds are also found, for instance 788 cm^{-1} in $LiNbO_3$,[36] or even below 600 cm^{-1} in Yb metalorganic complexes,[37] indicating a reduction of the CF strength on Yb^{3+}. In the latter case, a reduction of the effective Yb charge due to covalent bonds of oxygen to the neighboring organic ligands may contribute to the observed CF reduction, while in ionic crystals such CF strength reductions are partially ascribed to larger Yb^{3+} bond distances.

Even when the same Yb^{3+} coordination occurs in a given material the site symmetry influences the $^{2S+1}L_J$ multiplet splitting. Sesquioxides sharing 6-fold oxygen coordinated Yb^{3+} with and without a center of symmetry are a case similar to the present 0.3 at%Yb:CNGG that can guide us for the spectroscopic assignments. While efforts have been made in the assignment of usually experimentally incomplete Yb^{3+} energy level sets both for C_2 and C_{3i} Yb centers of cubic sesquioxides,[38,39] mainly through the application of the barycenter plot law,[34] only CF analyses of 24c dodecahedral Yb^{3+} energy levels have been attempted for garnet hosts.[40,41] These previously known data for cubic sesquioxides indicate that CF splittings of $^2F_{7/2}$ and $^2F_{5/2}$ are always wider and their corresponding barycenters are located at higher energies for centrosymmetric C_{3i} Yb^{3+} centers than for the C_2 ones, see Table 2 in ref. 38 and the ESI† (Table S1). The above indicated splittings for the C_{3i} 16a Yb^{3+} center in the 0.3 at%Yb:CNGG crystal are considerably larger than those of Yb^{3+} in the noncentrosymetric D_2 24c site in other garnet hosts, for instance, 766 cm^{-1} and 352 cm^{-1} for $^2F_{7/2}$ and $^2F_{5/2}$, respectively, in YbAG, or 624 cm^{-1} and 434 cm^{-1} for YbGG, see Table S2 (ESI†). It could be assumed that larger CF splitting amplitudes for the centrosymmetric C_{3i} 16a Yb^{3+} center are associated with the cooperative effect of considerably smaller bond distances for 16a Yb^{3+} than for Yb^{3+} in the dodecahedral environment as well as with an increase of the symmetry in the 16a center with regard to the 24c one.

The solubility limit for Yb^{3+} incorporation at 16a positions in the CNGG crystal is rather low, obviously below 0.3 at% of the dodecahedral site. From the facts that the background optical absorption at λ = 960.3 nm of dodecahedral Yb^{3+} centers in the 0.3 at%Yb:CNGG crystal is about 50% of the total, see Fig. 5, and that the total Yb content was estimated from OA comparison as 0.08 at% of the dodecahedral site, the Yb density in the octahedral 16a garnet site can be roughly estimated to be $\approx 5 \times 10^{18}$ cm^{-3}. Such a low limit is in fact expected due to the large Yb^{3+} ionic radii (0.868 Å for VI coordination) compared to those of Nb^{5+} and Ga^{3+} (0.64 Å and 0.62 Å, respectively, also for VI coordination). Due to the low solubility limit for Yb incorporation in the octahedral garnet site, direct evidence of corresponding MD transitions in the OA spectrum will diminish with the increase of Yb content in the crystal, and in fact the same OA bands from 16a Yb^{3+} can be also perceived with very low intensity in the 77 K OA spectrum of the 2 at%Yb:CNGG crystal reported by Voronko *et al.*,[25] while they are no longer observed in the OA spectrum of the 8 at%Yb:CNGG crystal, see Fig. 2b, since for these latter crystals ED transitions of Yb^{3+} in the dodecahedral garnet site have intensities several orders of magnitude stronger than those of the MD of Yb^{3+} in the octahedral garnet site.

Given that forced ED intraconfigurational f–f Ln^{3+} transitions from the centrosymmetric sites are strictly forbidden, the $^2F_{5/2} \rightarrow {}^2F_{7/2}$ emission from 16a Yb^{3+} has a predominant MD character. Consequently, Yb:CNGG is able to provide simultaneously well-differentiated sets of Yb^{3+} $^2F_{7/2} \leftrightarrow {}^2F_{5/2}$ ED and MD transitions, arising from 24c and 16a garnet sites, respectively.

The evaluation of the MD contribution of the 16a Yb^{3+} $^2F_{5/2}(0') \rightarrow {}^2F_{7/2}(1, 2, 3)$ (λ_{EMI} = 996.7, 1008.7 and 1080.6 nm) transitions can be performed by comparing the total decay rate derived from the measured lifetime value, $\Gamma_{total} = 1/\tau$, with the MD spontaneous emission rate, $A_{MD} = A'_{MD} \times n_r^3$, where the vacuum value A'_{MD} is predicted in ref. 12 and n_r = 1.96 is the measured refractive index for CNGG at $\lambda \approx$ 1000 nm.[14] The MD branching ratio, defined as $\beta_{MD} = A_{MD}/\Gamma_{total}$, results in $\beta_{MD} \approx$ 50% for 16a Yb^{3+} in CNGG if the room temperature center lifetime is taken as $\tau \approx$ 4 ms, see Fig. 4b. This value is similar to previous β_{MD} values indicated for the $^2F_{5/2}(0') \rightarrow {}^2F_{7/2}(0)$ Yb^{3+} emission in crystals hosting Yb^{3+} in lattice sites with a center of symmetry, such as SrF_2, Rb_2NaYF_6 or $ScBO_3$.[12] Such crystals are difficult to grow and are not easily available with specific Yb doping, while unfortunately the MD branching ratio of Yb^{3+} in standard YAG is only 10.8%.[12] Therefore, even though the 16a Yb^{3+} center is present in the CNGG garnet with a low density, the strong MD character of its transitions makes them observable, which highlights the interest of the 0.3 at%Yb:CNGG crystal to be used for probing local magnetic fields in plasmonic resonances and metamaterials.

5. Conclusions

A new centrosymmetric octahedral Yb^{3+} center has been identified in the disordered CaNbGa garnet crystal with spectroscopic properties clearly different, both at 6 K and 300 K, from the usual dodecahedral Yb^{3+} center found in this and similar garnets. This new center, which shows favorable properties to be used as a probe for the intensity of magnetic fields radiated by plasmonic structures, operates around λ = 1 μm which is a

good compromise for lithographic fabrication and optical detection techniques. It is characterized by $^2F_{7/2}(0–3)$ = 0, 290, 410, 1069 cm^{-1} and $^2F_{5/2}(0'–2')$ = 10 323, 10 413, 11 161 cm^{-1} Yb^{3+} m_J energy levels, which are consistent with the large CF splittings and barycenter energies expected for centrosymetric Yb^{3+} centers in ionic compounds, their individual positions being well reproduced by a CF simulation assuming a lower, but still with inversion center, D_{4h} symmetry.

The probe center can be operated at room temperature by excitation at λ = 960.3 nm and with best sensitivity detection near λ = 1080 nm, although other additional detection channels are found at λ = 998, 1011 and 1068 nm. The coexistence of dodecahedral and octahedral Yb^{3+} centers in the same crystal with roughly similar densities allows the detection of reference ED and signal MD PL contributions corresponding to the above centers, respectively. Separation of both contributions has been conveniently made by using time-resolved spectroscopy, since ED Yb^{3+} PL is short-lived ($\tau < 0.8$ ms) and the MD one is long-lived ($\tau \approx 4$ ms). The measured MD branching ratio in the studied garnet, $\beta \approx 50\%$, is equivalent to those previously reported in other centrosymmetric hosts, but the easy growth in air of the present CaNbGa garnet with congruent melting at ≈1470 °C will facilitate the fabrication of the required plasmonic or metamaterial structures in comparison for instance with Y_2O_3 whose crystal availability is very limited due to its high melting point of ≈2490 °C.

Conflicts of interest

There are no conflicts to declare.

Acknowledgements

This work has been supported by the Spanish Ministry of Economy and Competitiveness and by the European Regional Development Fund through project RTI2018-094859-B-I00. CSIC support for Open Access publication and advice of Prof. Rafael Valiente on time-resolved spectroscopic measurements are acknowledged.

References

1 W. T. Carnall, P. R. Fields and K. Rajnak, *J. Chem. Phys.*, 1968, **49**, 4424.
2 Q. Thommen and P. Mandel, *Opt. Lett.*, 2006, **31**, 1803.
3 N. Noginova, G. Zhu, M. Mavy and M. A. Noginov, *J. Appl. Phys.*, 2008, **103**, 07E901.
4 N. Noginova, Y. Barnakov, H. Li and M. A. Noginov, *Opt. Express*, 2009, **17**, 10767.
5 N. Yang, Y. Tang and A. E. Cohen, *Nano Today*, 2009, **4**, 269.
6 X. Ni, G. V. Naik, A. V. Kildishev, Y. Barnakov, A. Boltasseva and V. M. Shalaev, *Appl. Phys. B: Photophys. Laser Chem.*, 2011, **103**, 553.
7 T. H. Taminiau, S. Karaveli, N. F. van Hulst and R. Zia, *Nat. Commun.*, 2012, **3**, 979.
8 S. Karaveli and R. Zia, *Opt. Lett.*, 2010, **35**, 3318.
9 S. Karaveli and R. Zia, *Phys. Rev. Lett.*, 2011, **106**, 193004.
10 M. Kasperczyk, S. Person, D. Ananias, L. D. Carlos and L. Novotny, *Phys. Rev. Lett.*, 2015, **114**, 163903.
11 C. M. Dodson, J. A. Kurvits, D. Li, M. Jiang and R. Zia, *Opt. Mater. Express*, 2014, **4**, 2441.
12 C. M. Dodson and R. Zia, *Phys. Rev. B: Condens. Matter Mater. Phys.*, 2012, **86**, 125102.
13 L. DeLoach, S. Payne, L. Chase, L. Smith and W. Kway, *IEEE J. Quantum Electron.*, 1993, **29**, 1179.
14 E. Castellano-Hernández, M. D. Serrano, R. J. Jiménez-Riobóo, C. Cascales, C. Zaldo, A. Jezowski and P. A. Loiko, *Cryst. Growth Des.*, 2016, **16**, 1480.
15 S. Geller, *Z. Kristallogr.*, 1967, **125**, S1 (and refs. therein).
16 L. Suchow, M. Kokta and V. J. Flynn, *J. Solid State Chem.*, 1970, **2**, 137.
17 L. Suchow and R. Mondegarian, *J. Solid State Chem.*, 1973, **6**, 553.
18 B. V. Mill', *Sov. Phys. Crystallogr.*, 1975, **19**, 653.
19 M. Asano and J. A. Koningstein, *Chem. Phys.*, 1979, **42**, 369.
20 D. Lévy and J. Barbier, *Acta Crystallogr., Sect. C: Cryst. Struct. Commun.*, 1999, **55**, 1611.
21 M. O. Ramírez, L. E. Bausá, E. Cavalli and E. Bovero, *J. Appl. Phys.*, 2006, **99**, 013507.
22 H. G. Liu, W. C. Zheng and W. L. Feng, *Philos. Mag.*, 2008, **88**, 3075.
23 A. Kaminska, M. G. Brik, G. Boulon, M. Karbowiak and A. Suchocki, *J. Phys.: Condens. Matter*, 2010, **22**, 255501.
24 M. D. Serrano, J. O. Álvarez, C. Zaldo, J. Sanz, I. Sobrados, J. A. Alonso, C. Cascales, M. T. Fernández-Díaz and A. Jezowski, *J. Mater. Chem. C*, 2017, **5**, 11481.
25 Y. K. Voronko, A. V. Popov, A. A. Sobol and S. N. Ushakov, *Inorg. Mater.*, 2006, **42**, 1133.
26 V. E. Shukshin, *Phys. Wave Phenom.*, 2009, **17**, 165.
27 V. Lupei, A. Lupei, C. Gheorghe, L. Gheorghe, A. Achim and A. Ikesue, *J. Appl. Phys.*, 2012, **112**, 063110.
28 K. Shimamura, M. Timoshechkin, T. Sasaki, K. Hoshikawa and T. Fukuda, *J. Cryst. Growth*, 1993, **128**, 1021.
29 P. Porcher, M. C. dos Santos and O. Malta, *Phys. Chem. Chem. Phys.*, 1999, **1**, 397.
30 D. S. Sumida and T. Y. Fan, *Opt. Lett.*, 1994, **19**, 1343.
31 E. V. Zharikov, C. Zaldo and F. Díaz, *MRS Bull.*, 2009, **34**, 271 (and refs. therein).
32 J. Liu, X. Mateos, H. Zhang, J. Wang, M. Jiang, U. Griebner and V. Petrov, *Opt. Lett.*, 2005, **30**, 3162.
33 D. C. Brown, Z. Fleischman, L. D. Merkle, L. D. Sanjeewa, C. D. McMillen and J. W. Kolis, *Appl. Phys. B: Photophys. Laser Chem.*, 2020, **126**, 62.
34 P. Haumesser, R. Gaumé, B. Viana, E. Antic-Fidancev and D. Vivien, *J. Phys.: Condens. Matter*, 2001, **13**, 5427.
35 A. Lupei, G. Aka, E. Antic-Fidancev, B. Viana, D. Vivien and P. Aschehoug, *J. Phys.: Condens. Matter*, 2002, **14**, 1107.
36 E. Montoya, J. A. Sanz-García, J. Capmany, L. E. Bausá, A. Diening, T. Kellner and G. Huber, *J. Appl. Phys.*, 2000, **87**, 4056.

37 J. Wang, J. J. Zakrzewski, M. Heczko, M. Zychowicz, K. Nakagawa, K. Nakabayashi, B. Sieklucka, S. Chorazy and S. Ohkoshi, *J. Am. Chem. Soc.*, 2020, **142**, 3970 (and ref. 78 and 79 therein).
38 Y. Guyot, M. Guzik, G. Alombert-Goget, J. Pejchal, A. Yoshikawa, A. Ito, T. Goto and G. Boulon, *J. Lumin.*, 2016, **170**, 513.
39 E. Antic-Fidancev, J. Holsa and M. Lastusaari, *J. Phys.: Condens. Matter*, 2003, **15**, 863.
40 L. Hong-Gang, Z. Wen-Chen and F. Wen-Lin, *J. Lumin.*, 2010, **130**, 103.
41 L. Hong-Gang, G. Paweł and R. Czesław, *J. Lumin.*, 2011, **131**, 2690.

Electronic Supplementary Information

A probe of radiation field magnetic component based on octahedral Yb^{3+} in the CaNbGa garnet -CNGG- single crystal

*Jorge Omar Álvarez-Pérez, José María Cano-Torres, María Dolores Serrano, Concepción Cascales, Carlos Zaldo**

Instituto de Ciencia de Materiales de Madrid, Consejo Superior de Investigaciones Científicas, c/ Sor Juana Inés de la Cruz 3, 28049 Madrid, Spain.
*E-mail: cezaldo@icmm.csic.es

(i) Yb^{3+} Spectroscopy in Garnets

The Yb^{3+} spectroscopy in dodecahedral sites of garnets is quite well documented both in ordered crystals, such as $Y_3Al_5O_{12}$ –YAG–, and in other single crystal garnets with some degree of disorder. The optical absorption exhibits a well resolved 0-0′ transition near 970 nm (969 nm for YAG and 972 nm for CNGG≡ $\{Ca\square_D\}_3[Nb_{1-x}Ga_x\square_O]_2(Ga_{1-y}Nb_y\square_T)_3O_{12}$), but the resolution of 0-1′and 0-2′ ones is compromised by phonon coupling and inhomogeneous broadening associated to static random environments. Among the disordered garnets, CNGG has been particularly studied for its application as a mode-locked laser systems for ultrashort (fs) laser pulse production. The lanthanide absorption and emission bands are spectrally broadened, see Fig. ESI.1 for Yb doped crystals, due to the presence of vacancies (□) in the three crystallographic sites of the garnet structure as well as to the Nb^{5+} and Ga^{3+} simultaneous occupation of the octahedral and tetrahedral garnet sites, even though with specific occupancy factors. [*Kaminskii et al., Inorg. Mat. 22, 927, 1986*] Further, the crystal can be modified by the incorporation of Li^+ and Na^+, although each one plays a quite different role: Li exclusively incorporates in tetrahedral sites, while Na^+ is found exclusively in the dodecahedral site. Nevertheless, the similarity of the Yb^{3+} spectra in YAG and CNGG garnets shows that in both cases the common center is dodecahedral Yb^{3+}.

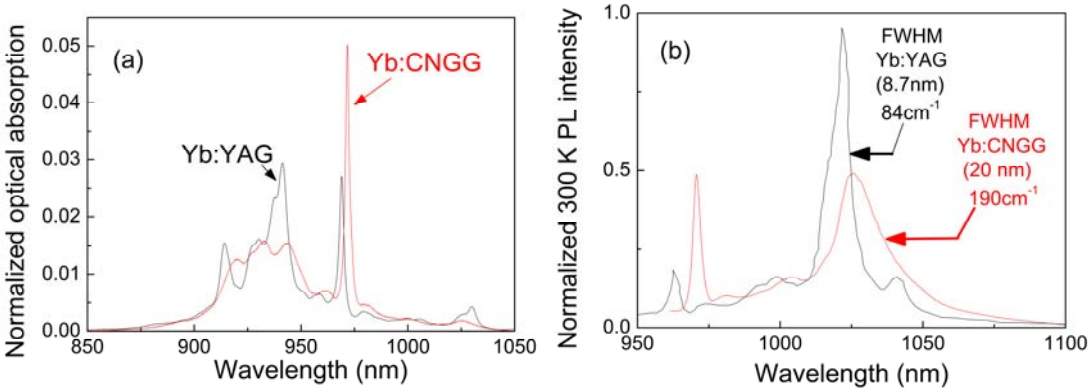

Fig. ESI.1 Comparison of the room temperature optical spectroscopy of Yb^{3+} in 5at%Yb:YAG (black lines) and in 8at%Yb:CNNG (red lines) single crystal garnets. All spectra are normalized to their total area equal to unity. (a) Optical absorption. (b) Photoluminescence excited in the 920-940 nm region.

Recently, a site selective excitation study resolved different dodecahedral Yb^{3+} sites in CNGG associated to the electric charge in the two edge-sharing nearby tetrahedra, i.e. either vacant or Li^{+}, Mg^{2+}, Ga^{3+} or Nb^{5+} occupancy, shifting the 0→0´ band to larger energy as the charge increases [*M. D. Serrano et al, J. Mat. Chem. C 5, 11481, 2017*]. Fig. ESI.2 shows evidence of these dodecahedral centers excited inside the 0-0´ Yb^{3+} linewidth (λ= 970-972 nm). The spectral distribution of the emission bands depends on the excitation wavelength. The excitation spectra of these emissions recorded in the 0.3at%Yb:CNGG crystal of interest in this work show bands at 960.3 nm and 968.7 nm in addition to the bands expected for the dodecahedral Yb, see Fig. ESI.2a, but interestingly the relative intensities of these two bands remain similar independently of the used λ_{EMI}, and they vary differently with regards to the intensity of the main peak at λ= 970.8 nm. These results from 6 K PL spectra indicate a same origin for OA bands at 960.3 nm and 968.7 nm, that is, they should correspond to $^2F_{7/2}(0)\rightarrow{}^2F_{5/2}(0', 1')$ electronic transitions associated to 16*a* Yb^{3+}, and furthermore the above four PL emission bands observed in Fig. 2 of the main text after excitation in any of these two bands should arise from 16*a* Yb^{3+} $^2F_{5/2}(0')\rightarrow{}^2F_{7/2}$ (n=0, 1, 2, 3) transitions.

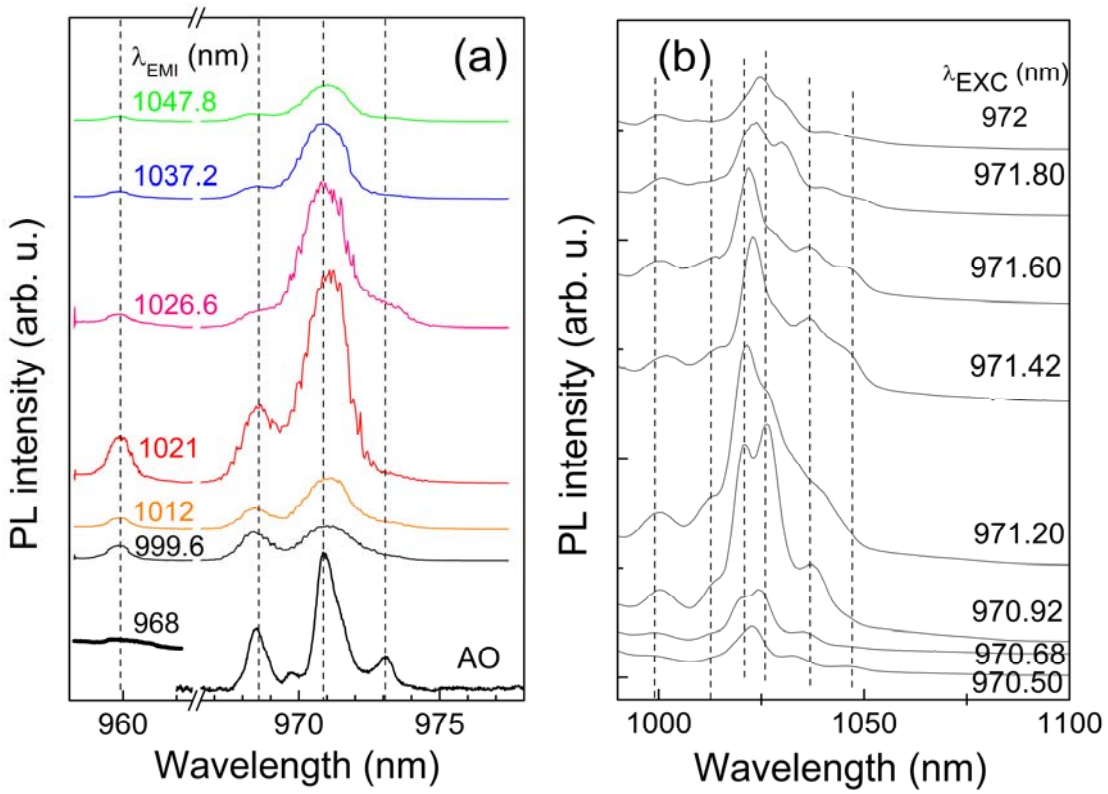

Fig. ESI.2 6 K photoluminescence spectra of 0.3at%Yb:CNGG crystal. (a) Comparison of the excitation spectra at several emission wavelengths λ_{EMI} with the 6 K optical absorption (AO) spectrum. (b) Photoluminescence emission for different excitation wavelengths inside the 0→0´ transition of dodecahedral Yb^{3+} centers.

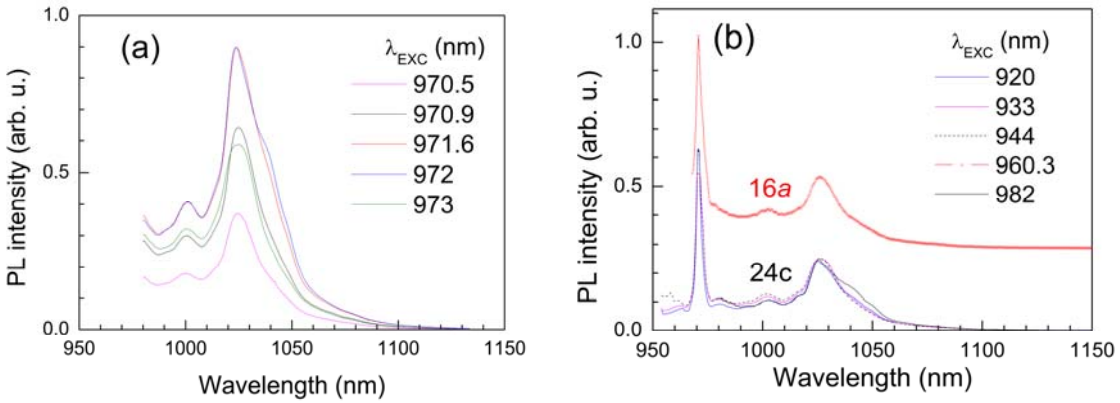

Fig. ESI.3 Room temperature photoluminescence of 0.3at%Yb:CNGG single crystal excited at different wavelengths. (a) PL excited at the inhomogeneously broadened $0 \rightarrow 0'$ dodecahedral Yb^{3+}. (b) Comparison of the PL corresponding to the octahedral Yb^{3+} center (excited at λ_{EXC}= 960.3 nm) with that corresponding to dodecahedral Yb^{3+} (excited at λ_{EXC}= 920, 933, 944 and 982 nm).

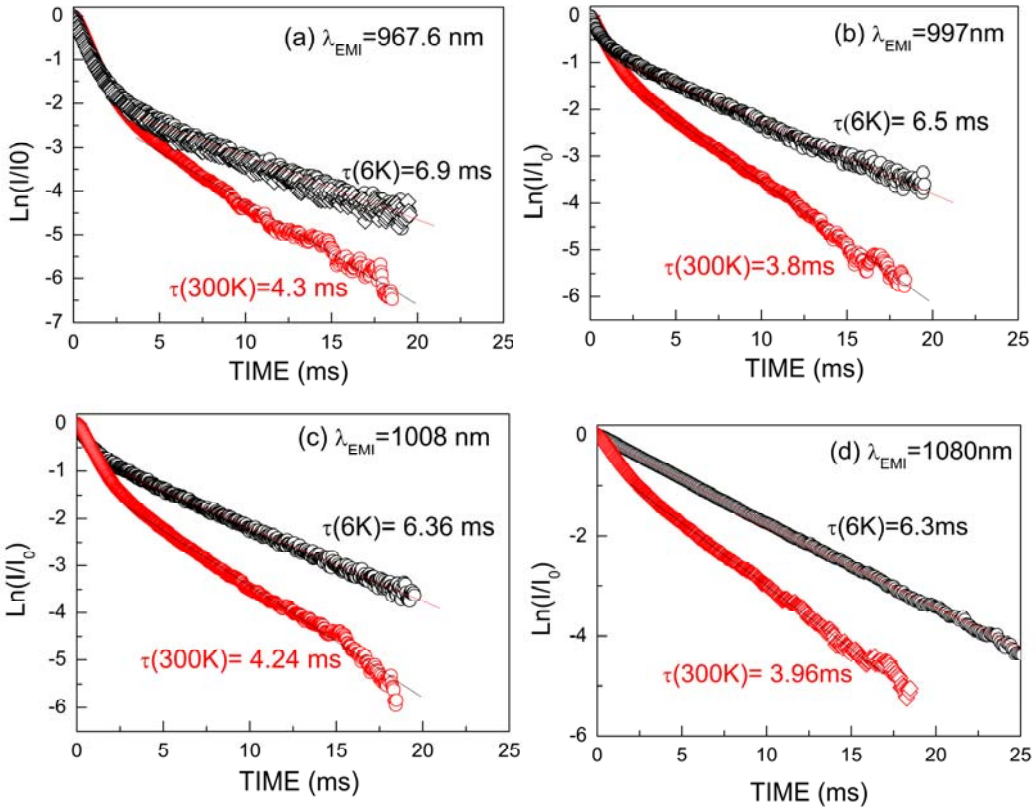

Fig. ESI.4 6 K photoluminescence intensity decay of the 16*a* Yb^{3+} $^2F_{5/2}$ multiplet of 0.3at%Yb:CNGG crystal, λ_{EXC}= 960.3 nm, and λ_{EMI} corresponding to transitions to different $^2F_{7/2}$ mJ energy levels. The circles are the experimental results and the lines are the exponential fits of the long component of the corresponding decay. (a) λ_{EMI}= 967.6 nm. (b) λ_{EMI}= 997 nm. (c) λ_{EMI}= 1008 nm. (d) λ_{EMI}= 1080 nm.

The room temperature time-integrated PL emission of dodecahedral Yb^{3+} in CNGG is little sensitive to the excitation wavelength. In addition to the 0′→0 emission at 972 nm two broad bands at about 1000 and 1025 nm are observed, see Fig. ESI.3. Further, the corresponding RT PL emission of the 16*a* octahedral Yb^{3+} is basically undistinguishable from that observed for the dodecahedral one. Apart from PL reabsorption, fast excitation diffusion between both center types may be responsible of this fact.

As explained in the main text, the PL of the octahedral 16*a* Yb^{3+} is characterized by a long time constant in the order of some ms. Fig. ESI.4 shows the 16*a* Yb^{3+} PL intensity decay kinetics (excited at λ= 960.3 nm) for several temperatures and emissions wavelengths associated to the emissions of the octahedral Yb^{3+} center. Results are quite independent of the monitored emission wavelength while the time constant decreases with increasing temperature.

Figs. ESI.5 and ESI.6 show some further information of the time-resolved PL results of 0.3at%Yb:CNGG crystal. Fig. 5a of the main text showed that optical absorptions of the dodecahedral and octahedral Yb centers in CNGG overlap at 960.3 nm. Fig. ESI.5 shows the low temperature (6 K) time-resolved PL excited at this wavelength after normalization to the most intense emission peak (λ= 1025 nm). The selection of long times for the analysis promotes the strength of the emissions assigned to the octahedral 16*a* Yb^{3+} center, λ= 968.7, 996.7, 1008.7 and 1080.6 nm. On the other hand, Fig. ESI.6 shows the comparison of the time-resolved PL of the octahedral center for low (6 K) and room temperatures. Although worse resolved at 300 K, the same bands are observed at both temperatures. The only noticeable change is the presence of a 1080 nm satellite band at 1068 nm, its origin was explained in the main text.

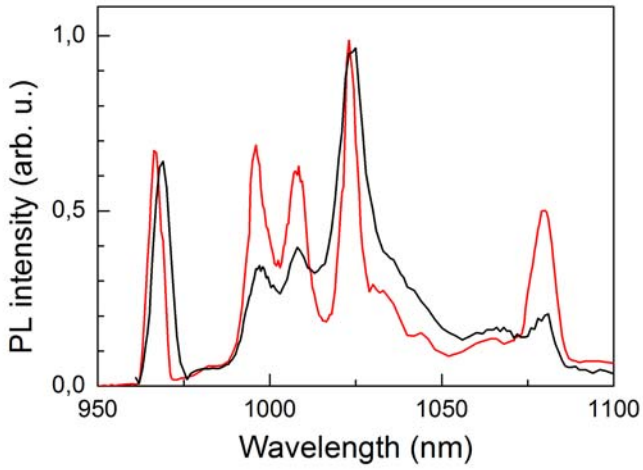

Fig. ESI.5 Comparison of the 6 K time-resolved PL contributions of dodecahedral (black line, delay 5 μs and gate width 250 μs) and octahedral (red line, delay 2.5 ms and gate width 8 ms) centers in 0.3at%Yb:CNGG. λ_{EXC}= 960.3 nm.

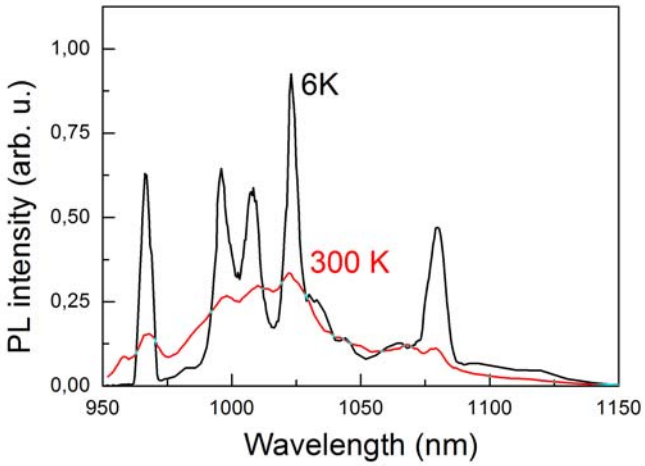

Fig. ESI.6 Comparison of the 6 K (black line) and 300 K (red line) time-resolved PL contributions of the octahedral center in 0.3at%Yb:CNGG. λ_{EXC}= 960.3 nm. Delay 2.5 ms and gate width 8 ms.

(ii) Crystal Field Analysis

The CF potential of the C_{3i} (≡ S_6) symmetry of the 16*a* site is described by nine non-zero CF parameters, $B_0^2, B_0^4, B_3^4, iB_3^4, B_0^6, B_3^6, iB_3^6, B_6^6$ and iB_6^6, which can be reduced to eight by a proper choice of the reference axis system, which cancels iB_3^4. The use of some calculation model for CF interactions to derive an initial set of C_{3i} CF parameters should be the usual first approach, however given the reduced number of energy levels of the Yb^{3+} configuration the modeling with such a large number of parameters is unrealistic. Instead, we start considering the undistorted octahedral (O_h) symmetry, and then the introduction of additional CF parameters will allow accounting for the distorted real symmetry ("descent of symmetry" method). To obtain an initial set of O_h CF parameters we applied the semi-empirical Simple Overlap Model (SOM), which estimates them from crystallographic positions and distances of oxygen ligands around 16*a* Yb^{3+}. After that, the calculation of the sequence of energy levels requires only two free-ion parameters, E^0, and the spin-orbit coupling constant, ζ, whose variation with the crystal host is theoretically predicted to be weak for a given Ln^{3+} ion, and consequently can be reasonably taken from the literature. These calculations were performed by using the program REEL [*P. Porcher, Fortran routines REEL and IMAGE for simulation of d^N and f^N configurations involving real and complex crystal-field parameters, unpublished*].

By choosing the threefold rotation axis as the *z*-axis, the O_h CF potential is described by the parameters $B_0^4, B_3^4, B_0^6, B_3^6$ and B_6^6, among which only B_0^4 and B_0^6 are independent parameters, since the B_3^4 / B_0^4, B_3^6 / B_0^6, and B_6^6 / B_0^6 ratios are symmetry restricted. [*C. Görller-Walrand and K. Binnemans, Rationalization of crystal-field parametrization, Handbook on the Physics and Chemistry of Rare Earths vol 23, eds. K. A. Gschneidner Jr. and L. Eyring (Amsterdam: North-Holland), 1996.*] Obtained SOM values for B_0^4 and B_0^6 were 1603.14 cm^{-1} and 75.58 cm^{-1}, respectively. Attempts of least square minimization fits of the experimental 16*a* Yb^{3+} energy levels (0 cm^{-1}, 290 cm^{-1}, 410 cm^{-1} and 1069 cm^{-1}, of the $^2F_{7/2}$ multiplet, and 10323 cm^{-1}, 10413 cm^{-1} and 11161

cm^{-1} of the excited $^2F_{5/2}$) to the calculated ones by using as starting CFPs the above trigonal set with SOM derived values were unsuccessful. Furthermore, the fit was also attempted by using as starting CF parameters the trigonal $B_0^2, B_0^4, B_3^4, B_0^6, B_3^6$ and B_6^6 set indicated for 16*a* Yb^{3+} in the $Na_3Sc_2V_3O_{12}$ garnet, [*Liu et al, Phyl. Magazine 88, 3075, 2008*] also with unsuccessful result.

Alternatively, if the fourfold rotation axis is chosen as the *z*-axis, the octahedral CF potential is described by the parameters B_0^4, B_4^4, B_0^6 and B_4^6, with B_0^4 and B_0^6 being the independent parameters, and the relationships $B_4^4/B_0^6 = \sqrt{5/14}$ and $B_4^6/B_0^6 = -\sqrt{7/2}$. By using the SOM values of this set of CF parameters the least squares minimization fit seemed to be much better than previously with the threefold axis as *z*-axis. Taking into account that the tetragonal bipyramid, with symmetry D_{4h}, is the higher symmetry polyhedron with coordination number CN=6 which can be considered as a distortion of the octahedron, and whose CF potential is described by tetragonal CF parameters, the following step was to include in the fitting process the effect of the additional B_0^2 to the earlier set of O_h CF parameters, to describe the D_{4h} CF potential, now with all CF parameters freely varying. All the 6 K experimentally determined 16*a* Yb^{3+} energy levels of CNGG were perfectly reproduced by using the set of D_{4h} CF parameters included in the Table 1 of the main text.

This centrosymmetric D_{4h} potential can be understood as the actual distortion of an "ideal" O_h octahedral symmetry around Yb^{3+}, by the removal of the C_3 symmetry axis, an effect that could be associated with some local modification, due to the structural disorder, in the neighborhood of the 16*a* Yb^{3+} site in this host.

(iii) ^2F_J crystal field splitting and the barycenter law

The $^{2S+1}L_J$ CF energy splitting, ΔE_J, was been shown to be linearly proportional to the scalar CF strength parameter N_J defined as [F. Auzel et al, *J. Physique*, 44, 201, 1983]

$$N_J = \left[\sum_k \sum_q \left(B_q^k\right)^2 \frac{4\pi}{2k+1} \right]^{1/2} . \qquad [1]$$

For the particular case of Yb^{3+}, $\Delta E(^2F_{7/2}) = 0.261 \times N_{7/2}$ holds. [*P. Haumesser et al., J. Phys.: Condens. Matter 13, 5427 2001*]

Using the CF parameters determined in Table 1, $N_{7/2} = 3569\ cm^{-1}$ is obtained for the CF strength of the 16*a* octahedral Yb^{3+} center in the 0.3at%Yb:CNGG crystal. This corresponds to a theoretical $\Delta E(^2F_{7/2}) = 931\ cm^{-1}$ which, taken into account that the constant relating ΔE_J and N_J is sensitive to the equidistance of the mJ sublevels,[*P. Haumesser et al., J. Phys.: Condens. Matter 13, 5427 2001*] supposes a good approximation of the 1069 cm^{-1} experimental value determined, and in any case it confirms the high CF strength on Yb^{3+} in the octahedral CNGG center.

Another test of confidence on the determined mJ levels is provided by the "barycenter law". [*P. Haumesser et al, J. Phys.: Condens. Matter 13, 5427, 2001*] It establishes a linear relationship between the barycenters ($\bar{E}$) of the energy positions of

mJ levels of different $^{2S+1}L_J$ multiplets. For the Yb^{3+} case it reads as $\bar{E}(^2F_{5/2}) = 10080 + 0.95\bar{E}(^2F_{7/2})$. This law is represented in Fig. ESI.7 along with the position of a large number of ionic compounds, including the position corresponding for the octahedral 16*a* Yb^{3+} center in CNGG which mJ energy levels were given in Table 1 of the main text.

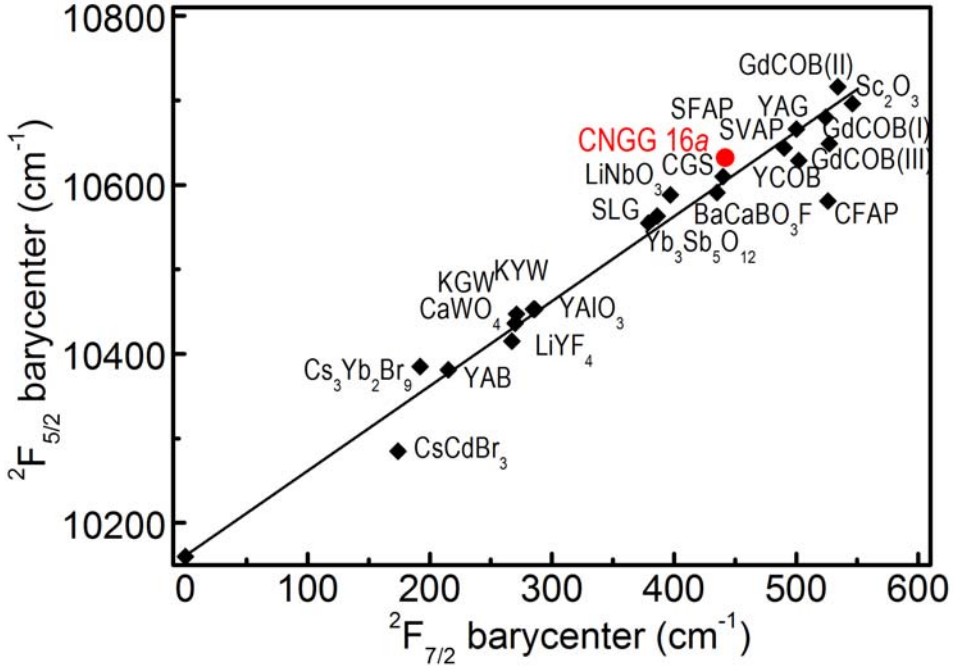

Fig. ESI.7 Plot of the barycenter energies of $^2F_{5/2}$ versus $^2F_{7/2}$ multiplets for several Yb-doped crystals (black diamonds). The line is a visual help. The red circle corresponds to the octahedral 16*a* Yb^{3+} center of the CNGG crystal.

For reference, Tables ESI.1 and ESI.2 provide values of ^2F_J splittings and barycenters for sexquioxides (Lu_2O_3) and garnets, respectively. In the first case including the comparison between centers with (C_{3i}) and without (C_2) center of symmetry.

Table ESI.1 Values of splittings and barycenters (in cm^{-1}) of six-fold oxygen coordinated Yb^{3+} for $^2F_{7/2}$ (0, 1, 2, 3) and $^2F_{5/2}$ (0', 1', 2') levels in C_2 and centrosymmetric C_{3i} centers of Lu_2O_3 [*Y. Guyot et al J. Lumin. 170, 513, 2016*]

Site symmetry	$^2F_{7/2}$		$^2F_{5/2}$	
	Splitting	Barycenter	Splitting	Barycenter
C_2	988	463	820	10620
C_{3i}	1193	588	1073	10738

Table ESI.2 Comparison of splitting and barycenter values (in cm^{-1}) of $^2F_{7/2}$ (0, 1, 2, 3) and $^2F_{5/2}$ (0', 1', 2') Yb^{3+} levels in octahedral CNGG site and in the usually determined dodecahedral garnet site for YAG= $Y_3Al_5O_{12}$, YbAG= $Yb_3Al_5O_{12}$, LuAG= $Lu_3Al_5O_{12}$, GGG= $Gd_3Ga_5O_{12}$, YGG= $Y_3Ga_5O_{12}$ and YbGG= $Yb_3Ga_5O_{12}$. Ref 1 : [*G. A. Bogomolova et al, Sov. Phys. JETP 42, 440, 1976*]. Ref 2: [*R. A. Buchanan et al, Phys. Rev. 159, 245, 1967*]. Ref. 3: [*A. Brenier et al, J. Opt. Soc. Am. B 23, 676, 2006*]. Ref. 4: [*Liu Hong-Gang et al, J. Lum. 131, 2690, 2011*]. Ref 5: [*Y. Guyot et al, Opt. Mater. 27, 1658, 2005*].

Garnet host	$^2F_{7/2}$		$^2F_{5/2}$		Reference
	Splitting	Barycenter	Splitting	Barycenter	
YAG	785	490.5	352	10543.3	1
YAG	782	500.8	353	10538.3	2
YAG	786	496.5	600	10629.3	3
YbAG	766	521.3	352	10549.3	4
LuAG	762	499.3	570	10625.0	3
GGG	657	414.8	502	10567.3	5
YGG	642	446	428	10546.0	1
YbGG	624	-	434	10559.7	2
CNGG	1069	442	838	10632	This work